Simulation Modelling Practice and Theory 104 (2020) 102141

Contents lists available at ScienceDirect

Simulation Modelling Practice and Theory

journal homepage: www.elsevier.com/locate/simpat

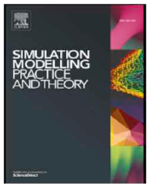

Finite element simulation-based predictive regression modeling and optimum solution for grain size in machining of Ti6Al4V alloy: Influence of tool geometry and cutting conditions

Morteza Sadeghifar[a,*], Mahshad Javidikia[b], Victor Songmene[b], Mohammad Jahazi[b]

[a] *Department of Mechanical, Industrial and Aerospace Engineering, Concordia University, Montreal, QC, Canada*
[b] *Department of Mechanical Engineering, École de Technologie Supérieure, Montreal, QC, Canada*

Authors' accepted manuscript
Article published in *Simulation Modelling Practice and Theory*, Volume 104, November 2020, 102141
https://doi.org/10.1016/j.simpat.2020.102141

Finite Element Simulation-Based Predictive Regression Modeling and Optimum Solution for Grain Size in Machining of Ti6Al4V Alloy: Influence of Tool Geometry and Cutting Conditions

Morteza Sadeghifar[a,*], Mahshad Javidikia[b], Victor Songmene[b], Mohammad Jahazi[b]

[a]*Department of Mechanical, Industrial and Aerospace Engineering, Concordia University, Montreal, Canada*
[b]*Department of Mechanical Engineering, École de Technologie Supérieure, Montreal, Canada*
* Corresponding author. *E-mail address: sadeghifar.morteza@gmail.com*

Abstract

The present research study was aimed at studying the impact of machining parameters on grain size alterations in machining of Ti6Al4V alloy using finite element analysis (FEA) based on the Johnson-Mehl-Avrami-Kolmogorov (JMAK) recrystallization model. The machining parameters consist of both cutting conditions and tool geometry including cutting speed, feed rate, tool edge radius and rake angle. Three series of JMAK constants were used in the simulations and the degree of accuracy of the obtained results were compared. Finite element (FE) simulations were conducted for machining conditions designed using a D-optimal Design of Experiment (DoE). Analysis of Variance (ANOVA) was carried out to identify the most effective machining parameters on the responses of average grain size (AGS), machining temperature (MT), cutting force (CF), and feed force (FF). Next, Response Surface Method (RSM) was used to predict regression models of AGS, MT, CF, and FF. The optimal values of machining parameters were obtained to improve AGS, MT, CF, and FF. The ANOVA results showed that rake angle and cutting speed were, respectively, the most and least significant parameters affecting AGS in the design space. Rake angle was the most effective parameter influencing all of the responses. The single-criterion optimization of AGS provided a small improvement in AGS with a high increase in material removal rate (MRR). The results of the multi-criteria optimization of AGS, MT, CF, and FF demonstrated that machining of Ti6Al4V alloy with a tool having a medium cutting edge radius and high positive rake angle at a medium cutting speed and a low feed rate in the design space produced finer grains along with reduced CF and FF and unchanged MT.

Keywords: *Grain Size . Machining Characteristics . FE Simulation . Regression Modeling . Optimum Solution*

Authors' accepted manuscript
Article published in *Simulation Modelling Practice and Theory*, Volume 104, November 2020, 102141
https://doi.org/10.1016/j.simpat.2020.102141

1. Introduction

Surface integrity including surface roughness, residual stresses, and microstructural alterations has experimentally been studied and modeled in machining processes during last decades as it significantly affects the fatigue life and corrosion resistance of machined components [1,2]. Machining parameters including cutting conditions and tool geometry greatly affect surface integrity characteristics [1,3]. The required materials, tools, and equipment to conduct experimental tests are costly and the procedure to set up the tests is often time consuming. Finite Element modeling of cutting-induced residual stresses has been studied by many researchers [1]; however, in contrast, only a small number of FE simulation studies on microstructural alterations including grain size variations are available in orthogonal machining of metals [4-8]. This could be due to the complexity in accurately predicting the thermo-mechanical evolution of the microstructure during machining operations.

In 2014, Rotella and Umbrello [4] investigated the grain size and the hardness modifications in dry and cryogenic cuttings of Ti6Al4V alloy based on the Zener-Hollomon and Hall-Petch equations using the DEFORM^{TM} software. The results showed that increasing cutting speed and feed rate reduced grain size. Ding and Shin [9] utilized a dislocation density-based material plasticity model to simulate the grain size refinement during orthogonal cutting of a commercially pure titanium (CP Ti) material using the Abaqus® software. They predicted grain size by calibrating the temperature-dependent dislocation model's control parameters.

Liu et al. [10] used a microstructure evolution model to simulate orthogonal cutting of OFHC copper for several cutting speeds using the AdvantEdge^{TM} software. The results showed that the model predicted significant grain refinement over large regions in the vicinity and within the primary shear zone (PSZ) and in the chip. Jafarian et al. [11] identified the Johnson-Cook material constants of Inconel 718 using orthogonal cutting and examined the effect of tool geometry on microstructural changes using the DEFORM^{TM} FE code. The results showed that increasing both chamfer angle and hone radius increased surface hardness and decreased surface grain size. They also reported that the depth of the affected layer was more sensitive to the tool edge type than to the geometrical parameters of each tool.

Wang et al. [6] simulated the evolution of grain size and microhardness during high speed orthogonal machining of Ti6Al4V alloy based on the Zener-Hollomon and Hall-Petch equations using the Abaqus® FE code. They found that the depth of machining deformation zone remained almost constant with cutting speed, while grain size and microhardness changed inversely with cutting speed. Pan et al. [7] investigated the effect of machining parameters including cutting speed and feed rate on microstructural changes in orthogonal machining of Ti6Al4V based on the JMAK model using the DEFORM^{TM}

software. They found that a higher cutting speed decreased the grain size of the machined surface in high speed machining.

Caruso et al. [12] predicted the variations of the grain size and hardness in the surface and subsurface of machined components of Waspaloy based on the Zener-Hollomon and Hall-Petch equations using the DEFORM^{TM} software. They found that both cutting speed and feed rate affected the machined surface and subsurface integrity. Wu et al. [13] examined the effects of micro-grooved cutting tools on grain size distributions in orthogonal cutting of Al6061-T6 alloy based on FEM using the Abaqus$^{®}$ software. The results showed that the micro-groove width and convex width changed the grain size along the depth from the machined surface and the depth from the tool-chip interface.

In a recent publication, Yameogo et al. [8] utilized the JMAK model to predict cutting forces, chip morphology and the volume fraction of dynamically recrystallized grains in orthogonal turning of Ti6Al4V alloy using the Abaqus$^{®}$ software. Good agreement was observed between the simulated and measured results; however, no prediction of grain size was presented. Jafarian et al. [14] implemented a grain size-based flow stress model into the DEFORM^{TM} software to take into account the influence of changes in material properties in orthogonal turning of Inconel 718. They observed that the dynamic events in the material model modified the material behavior during the cutting process, and consequently, improved the accuracy of grain size predictions.

The above review of the literature shows that a comprehensive analysis of machining-induced grain size in terms of both tool geometry and cutting conditions using FE-based predictive regression modeling and design optimization study is missing in the literature. Accordingly, the main objective of the present research was to fill the aforementioned gap in the knowledge of machining-induced microstructural alterations based on FEA, which would allow avoiding conducting expensive, time-consuming experimental machining tests and subsequent grain size measurements. To achieve this, the surface and subsurface grain sizes were predicted based on the JMAK model using the DEFORM^{TM} software and the impact of the selected set of constants on the results were determined and their physical meanings were discussed. In addition, the most effective machining parameters including cutting speed, feed rate, tool edge radius and rake angle on AGS, MT, CF, and FF were identified using ANOVA and the optimal machining parameters were captured to reduce AGS along with MT, CF, and FF using optimization studies.

2. FE simulations of cutting process and microstructure alterations

In the following, the formulation and the characteristics of the FE model are briefly explained. The equations of motion during cutting can be expressed at a specific instant of time as [15]:

$$[M]\{\ddot{U}\} + \{R_{\text{int}}\} = \{R_{ext}\} \tag{1}$$

where $[M]$ is the mass matrix, $\{\ddot{U}\}$ is the acceleration vector ($\{U\}$ is the displacement), and $\{R_{\text{int}}\}$ and $\{R_{ext}\}$ are the vectors of internal and external forces, respectively. The influence of damping is neglected, and therefore, $\{R_{\text{int}}\}$ equals:

$$\{R_{\text{int}}\} = [C_d]\{\dot{U}\} + [K_s]\{U\} \cong [K_s]\{U\} \text{ where } [C_d] \cong 0 \tag{2}$$

in which $[C_d]$ and $[K_s]$ are the damping and stiffness matrices, respectively. $\{R_{ext}\}$ involves the external forces applied during cutting including the reaction forces at the supports.

Heat transfer occurring during the machining process is expressed as [15]:

$$[C_T]\{\dot{T}\} + [K_T]\{T\} = \{\dot{Q}_g\} \tag{3}$$

where $[C_T]$ and $[K_T]$ are the volumetric heat capacitance and thermal conduction matrices, respectively. $\{\dot{Q}_g\}$ is also the total heat generation in the machining process.

The thermal contact between the tool and workpiece was defined using the heat conduction through the tool-chip contact face from the chip to the tool during the cutting process which is calculated as [15]:

$$Q = h_{\text{int}}\,(T_{wp} - T_t) \tag{4}$$

where h_{int} is heat transfer coefficient, T_{wp} and T_t are the workpiece and tool's temperature at the tool-chip interface. A heat transfer coefficient of 10^7 $W/m^2\,{}^oC$ was calibrated for modeling and an initial temperature of 20 ${}^oC$ (room temperature) was applied to both tool and workpiece. It needs mentioning that the heat transfer coefficient was calibrated when the steady-state condition for cutting temperature was reached. The high value was selected because the high pressure of the chip on the tool rake face makes a perfect contact between the tool and chip [1]. Another reason was to quickly reach the steady-state condition in order to shorten the cutting time and avoid excessive distortion of elements [1]. Most importantly, this high value provided good agreement between the experimental and predicted average grain sizes.

The Johnson-Cook material constitutive model was used to model plastic deformation of the workpiece material as follows:

$$\sigma_{fl} = [A + B(\varepsilon)^n]\left[1 + C\ln\left(\frac{\dot{\varepsilon}}{\dot{\varepsilon}_0}\right)\right]\left[1 - \left(\frac{T - T_{room}}{T_{melt} - T_{room}}\right)^m\right] \tag{5}$$

where σ_{fl} is the flow stress of the workpiece material, ε is the plastic strain, $\dot{\varepsilon}$ the plastic strain rate (s^{-1}), $\dot{\varepsilon}_0$ the reference plastic strain rate (s^{-1}), $T\,({}^oC)$ the workpiece temperature, $T_{melt}\,({}^oC)$ the melting temperature of the workpiece, and $T_{room}({}^oC)$ the room temperature. Moreover, A (MPa) is the initial yield strength, B (MPa) the hardening modulus, C the strain rate sensitivity coefficient, n the hardening coefficient, and m the thermal softening coefficient. The microstructure of Ti6Al4V alloy is composed of α grains with low concentration of β ones, where the volume fraction of α phase is 95% [7], which is dominant. As a result, β phase was ignored in FE simulations [6,7]. The Johnson-Cook constants of Ti6Al4V alloy based on α phase given in Table 1 were utilized in the present study.

The mechanical contact between the tool and the workpiece was modeled using the shear friction model as follows [16]:

$$\tau = m_f \tau_{Chip} \tag{6}$$

where m_f is the shear friction coefficient and τ_{Chip} is the shear flow stress in the chip at the tool-chip interface. A shear friction model with the coefficient of 0.9 was used by calibrating and comparing the present simulated average grain sizes with the experimental ones obtained by Ref. [7].

A rectangular workpiece with the length of 4.75 mm and the width of 1.12 mm was created in the DEFORM^{TM} software. 4-node elements with bilinear displacement and temperature were utilized to mesh the workpiece and tool. The tool was much stiffer than the workpiece and was modeled as a rigid body [16,17]. The workpiece and tool's material properties are listed in Table 2. The thermal and mechanical Boundary Conditions (BCs) were prescribed as displayed in Fig. 1. The top and right sides of the cutting tool were fixed in the horizontal and vertical directions ($V_x = 0$ and $V_y = 0$, respectively). The workpiece material moves towards the fixed tool in the horizontal direction. The bottom and left sides of the workpiece were also fixed in the vertical direction ($V_y = 0$). The sides of the workpiece and tool being far from the cutting zone were retained at ambient temperature 20 ^oC (T_{room}) [16]. Based on the experimental observations of chips in Ref. [7], segmented chips were simulated using the Cockroft-Latham's criterion as [7]:

$$\int_0^{\varepsilon_f} \sigma_1 \, d\varepsilon = D \tag{7}$$

where ε_f is the effective strain, σ_1 is the maximum principle stress, and D is the material fracture constant. According to Eq. (7), the fracture occurs and chip segmentation starts once the integral reaches the fracture constant. D was set to 200 based on the data reported in [7]. This value is often obtained using calibration of the FE model by matching the predicted results with the experimental ones.

Table 1 The Johnson-Cook material constants of Ti6Al4V alloy [7]

$A\ (MPa)$	$B\ (MPa)$	n	C	m	$T_{melt}\ (^{o}C)$	$T_{room}\ (^{o}C)$
889.65	683.1	0.47	0.035	1	1649	20

Table 2 Mechanical and thermal properties of the workpiece and tool [7]

Properties	Ti6Al4V	WC-CO
Density $\rho\ (kg/m^3)$	4430	15700
Young's modulus $E\ (MPa)$	$0.714\,T+113.34\times10^3$	560000
Poisson's ratio υ	0.34	0.25
Thermal conductivity $k\ (W/m\ ^{o}C)$	$7.039\ exp(0.0011T)$	26.7
Specific heat capacity $c\ (J/kg\ ^{o}C)$	$505.64\ exp(0.0007T)$	140.7
Thermal expansion coefficient $\alpha\ (1/\ ^{o}C)$	$3\times10^{-9}\,T+7\times10^{-6}$	4.7×10^{-6}

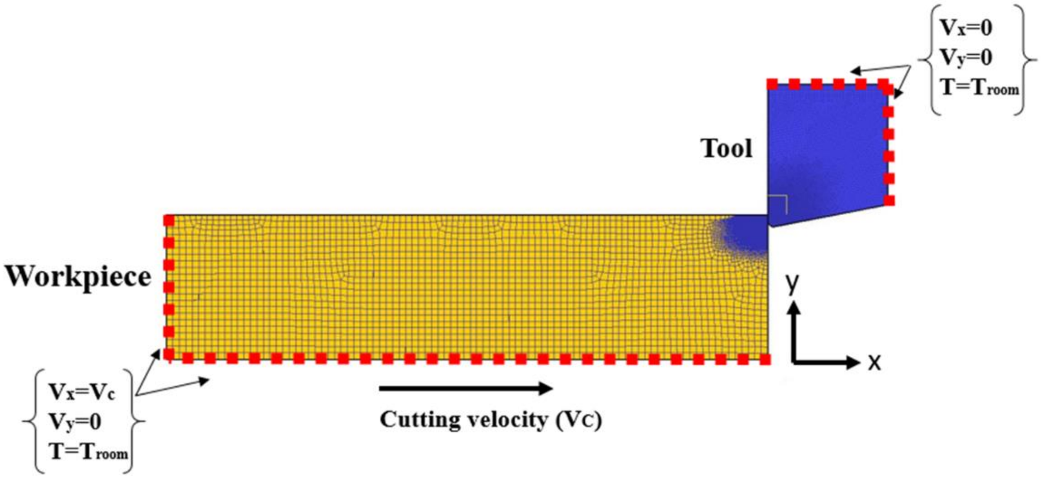

Fig. 1. The thermal and mechanical boundary conditions of the workpiece and tool.

The JAMK recrystallization model implemented in the DEFORM^{TM} software can be utilized to simulate microstructural alterations and define the transformation kinetics in a material [18]. Specific modules including Grain Growth and Static, Meta-dynamic, and Dynamic Recrystallizations may be used to predict microstructural alterations. The temperature, strain, strain rate, activation energies and initial grain size information in these modules are the input parameters for modeling purposes. Using the JMAK model, peak strain (ε_P), dynamic recrystallized volume fractions (X_{DRx}), dynamic recrystallized grain size (d_{DRx}), and average grain size (d_{avg}) can be predicted. Dynamic recrystallization generally occurs when a critical strain ε_c is reached. The latter is a function of the peak strain ε_p, i.e. $\varepsilon_c = a_2(\varepsilon_p)$, where a_2 is an Avrami constant, which is given as [5,7]:

$$\varepsilon_p = a_1 d_0^{h_1} \dot{\varepsilon}^{m_1} \exp(Q_{act} m_1/RT) + c_1 \tag{8}$$

where R is the gas constant, Q_{act} is the activation energy, a_1, h_1, m_1, and c_1 are material constants. The dynamic recrystallization and the fraction of dynamically recrystallized grains are defined using the Avrami equation as follows [5,7]:

$$X_{DRx} = 1 - \exp\left[-\beta_d \left(\frac{\varepsilon - a_{10}\varepsilon_p}{\varepsilon_{0.5}}\right)^{k_d}\right] \tag{9}$$

in which ε is the strain, ε_p is the peak strain, and X_{DRx} is the volume fraction of dynamically recrystallized material. $\varepsilon_{0.5}$ is the strain for X_{DRx}= 0.5, and is expressed as:

$$\varepsilon_{0.5} = a_5 d_0^{h_5} \varepsilon^{n_5} \dot{\varepsilon}^{m_5} \exp(Q_{act} m_5/RT) + c_5 \tag{10}$$

where d_0 is the initial diameter of the grains, and a_5, h_5, n_5, m_5, and c_5 are the Avrami material constants. The dynamically recrystallized grain size is then obtained by [5,7]:

$$d_{DRx} = a_8 d_0^{h_8} \varepsilon^{n_8} \dot{\varepsilon}^{m_8} \exp(Q_{act} m_8/RT) + c_8 \tag{11}$$

where a_8, h_8, n_8, m_8, and c_8 are the Avrami material constants. Average grain size is calculated based on the mixture rule as follows:

$$d_{avg} = d_0(1 - X_{DRx}) + d_{DRx} X_{DRx} \tag{12}$$

In the present work, an initial average grain size of d_0=15 μm, which was experimentally measured by Ref. [7], was used for FE predictions. It is well recognized that in thermal-mechanical operations of metals such as machining, the thermal recovery/recrystallization generally starts at the temperature limit (T_{lim}) of (0.4-0.5)×T_m. Consequently, the dynamic recrystallization occurs in the regions of such temperatures [5]. It should be noted that phase transformation does not occur on the machined surface during the cutting process as the maximum temperature on the machined surface does not reach the phase transformation temperature of 980 ^oC. Figure 2 shows how the grain size can be simulated using the JMAK model.

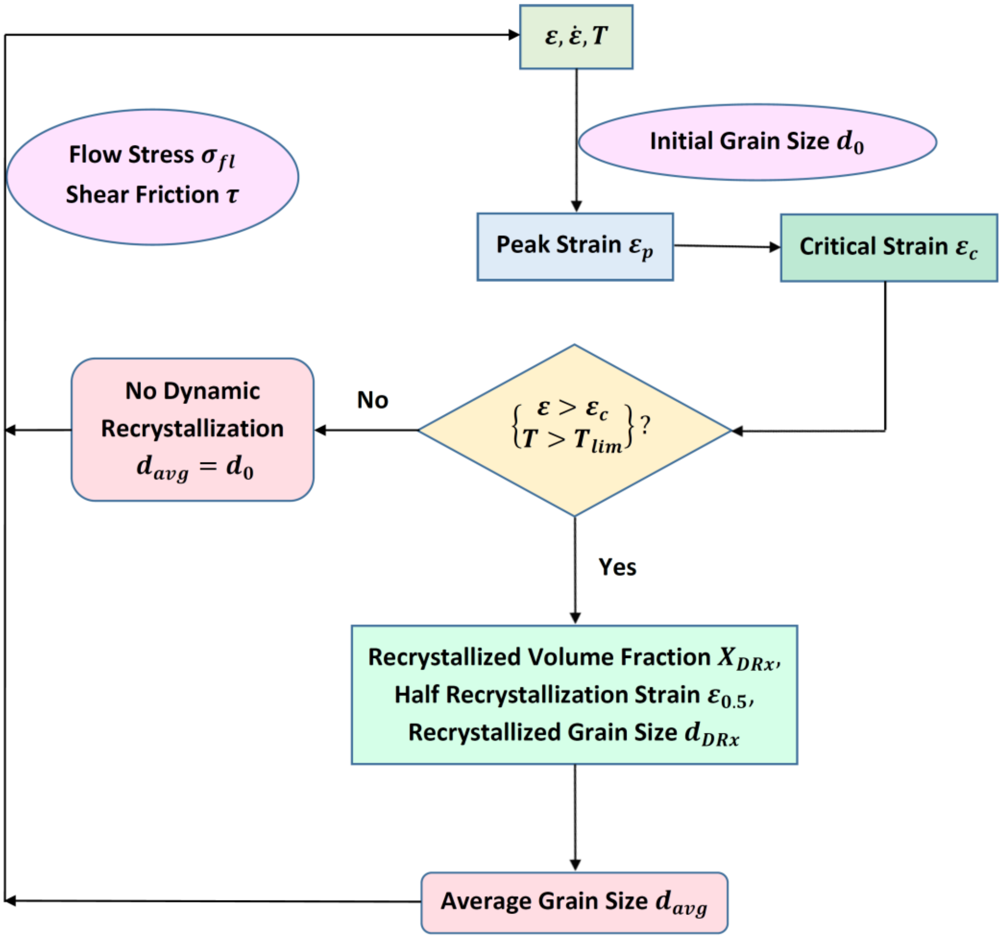

Fig. 2. A flowchart showing how the grain size alteration is modeled in the FE simulations.

3. Validation of the finite element model

The developed finite element model was validated by comparing the present simulated average grain sizes with the measured ones given by Ref. [7]. In this study, the grain sizes were simulated using three JMAK constants called JMAK 1, JMAK 2, and JMAK 3 (given in Table 3) provided by Pan et al. [7], Yameogo et al. [8], and Arisoy et al. [5], respectively. Two machining parameters presented in Ref. [7] and listed in Table 4, were utilized for FE validations. The FE model of the cutting process for Test No. 2 is displayed in Fig. 3. Four mesh windows were assigned to the workpiece in order to have a high-quality fine mesh especially in the machined workpiece's surface and near-surface. This assisted to have accurate microstructural predictions in the machined surface and subsurface. It needs mentioning that the valid zone in the workpiece to extract AGS in the FE simulations is the mid-length of the machined surface. This selected zone is far enough not only from the chip root to exclude the local effect produced by the tool's cutting edge at the chip root, but also from the right edge of the workpiece to avoid the influence of the boundary condition as well as the transient effects in the beginning of the cutting process. Another reason for choosing the mid-length zone of the workpiece is to have enough cutting length to reach the steady-state condition [1]. As viewed in Table 5, good agreement is observed between the present predictions for all the JMAK constants and the experimental results.

Table 3 Three JMAK constants utilized in the previous studies

Reference		Peak strain					
		a_1	h_1	m_1	$m_1 \times Q_{act}$	c_1	a_2
[7]	JMAK 1	0.0064	0	0.0801	30579 J/mol	0	0.8
[8]	JMAK 2	0.8	0	0.01	2180 J/mol	0	0.4
[5]	JMAK 3	2	0	0.006	1308 J/mol	0	0.8

Reference		DRx kinetics								
		a_5	h_5	n_5	m_5	$m_5 \times Q_{act}$	β_d	c_5	k_d	a_{10}
[7]	JMAK 1	0.022	0	0	0.11146	26430 J/mol	0.9339	0	0.5994	0.0311
[8]	JMAK 2	0.022	0	0	0.03	6540 J/mol	2	0	2	0.4
[5]	JMAK 3	1.21×10^{-5}	0.13	0	0.04	8720 J/mol	0.693	0	2	0

Reference		DRx grain size					
		a_8	h_8	n_8	m_8	$m_8 \times Q_{act}$	c_8
[7]	JMAK 1	150	0	0	-0.03	-6540	0
[8]	JMAK 2	150	0	0	-0.03	-6540	0
[5]	JMAK 3	150	0	0	-0.03	-6540	0

Table 4 Cutting conditions and tool geometry utilized for FE validations [7]

Test No.	Cutting speed $V(m/min)$	Feed rate $f(mm/rev)$	Edge radius $r_\beta(mm)$	Rake angle $\gamma_0(deg)$	Clearance angle $\alpha_0(deg)$
1	55	0.1	0.005	0	5
2	90	0.05	0.005	0	5

Table 5 Validation of the FE model using three different JMAK constants

	Average grain size $[\mu m]$			
Test No.	Measured by [7]	Predicted by the present study using:		
		JMAK 1	JMAK 2	JMAK 3
1	13.6	14.5	13.3	13.2
2	13.6	14.1	13.7	13.8

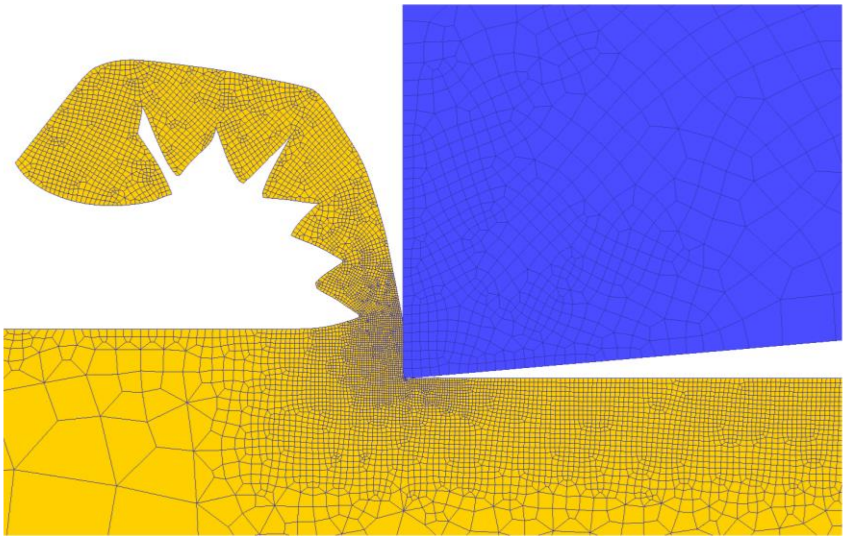

Fig. 3. The FE model of the cutting process for Test No. 2.

4. Results and discussions

4.1. Influence of JMAK constants

The predicted average grain size distribution in the machined surface and subsurface regions of the workpiece for two different cutting conditions called Test Nos. 1 and 2 are displayed in Fig. 4. As observed, AGS predicted using JMAK 1 were higher than those obtained with JMAK 2 and JMAK 3 for both cutting conditions. In addition, a study of the variation of the grain size with respect to the depth below the machined surface was carried out by tracking some nodes called P1, P2, etc. in the FE model from the machined surface to the bulk of the material. As seen in the diagrams in Fig. 4, for all the JMAK constants, AGS increased from 14.5, 13.3, and 13.2 μm at the surface for Test No. 1 and from 14.1, 13.7, and 13.8 μm at the surface for Test No. 2, to the depth of the workpiece where the grain size reached its initial value of 15 μm.

The data presented in Table 3 shows that the JMAK constants for the dynamically recrystallized (DRx) grain size were the same for all the three references. According to Eq. (11), since h_8 and n_8 are equal to zero, the dynamically recrystallized grain size d_{DRx} is independent of the initial grain size d_0 and the strain ε in the workpiece during cutting. In contrast, d_{DRx} is a function of the strain rate $\dot{\varepsilon}$ and temperature T. Since $Q_{act}m_8$ is negative, and R and a_8 are positive, the expression $\exp(Q_{act}m_8/RT)$, and consequently, d_{DRx} increase with increasing temperature. In contrast, since m_8 is negative, the term $\dot{\varepsilon}^{m_8}$, and as a result, d_{DRx} decrease with increasing strain rate. Therefore, the concomitant effects of temperature and strain rate determine the final value of d_{DRx}. However, average grain size d_{avg}

(a)

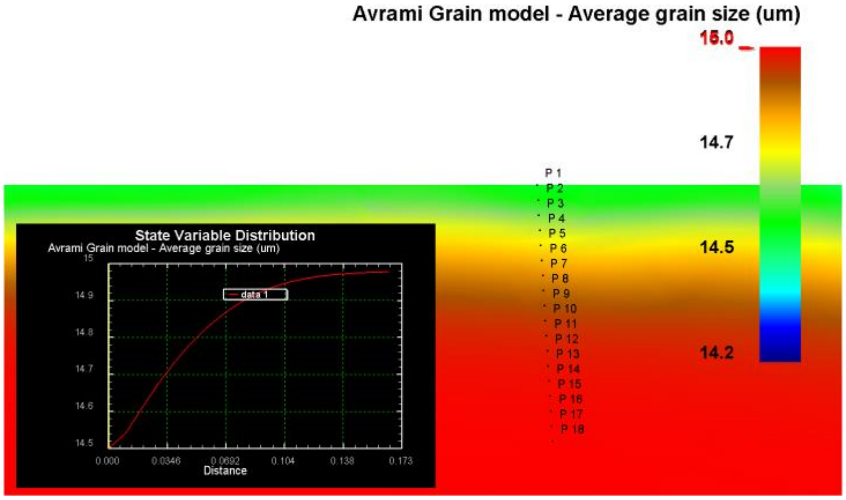
Avrami Grain model - Average grain size (um)
15.0
14.7
14.5
14.2
P 1
P 2
P 3
P 4
P 5
P 6
P 7
P 8
P 9
P 10
P 11
P 12
P 13
P 14
P 15
P 16
P 17
P 18
State Variable Distribution
Avrami Grain model - Average grain size (um)
15
14.9
14.8
14.7
14.6
14.5
data 1
0.000
0.0346
0.0692
0.104
0.138
0.173
Distance

(b)

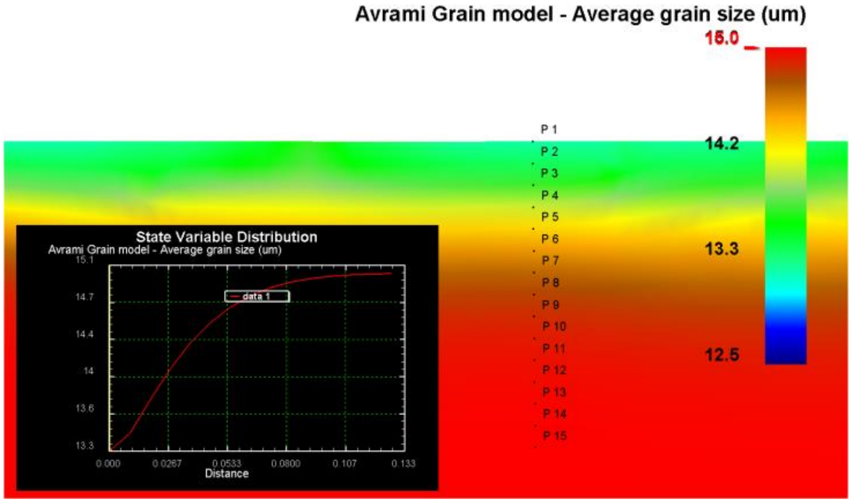
Avrami Grain model - Average grain size (um)
15.0
14.2
13.3
12.5
P 1
P 2
P 3
P 4
P 5
P 6
P 7
P 8
P 9
P 10
P 11
P 12
P 13
P 14
P 15
State Variable Distribution
Avrami Grain model - Average grain size (um)
15.1
14.7
14.4
14
13.6
13.3
data 1
0.000
0.0267
0.0533
0.0800
0.107
0.133
Distance

(c)

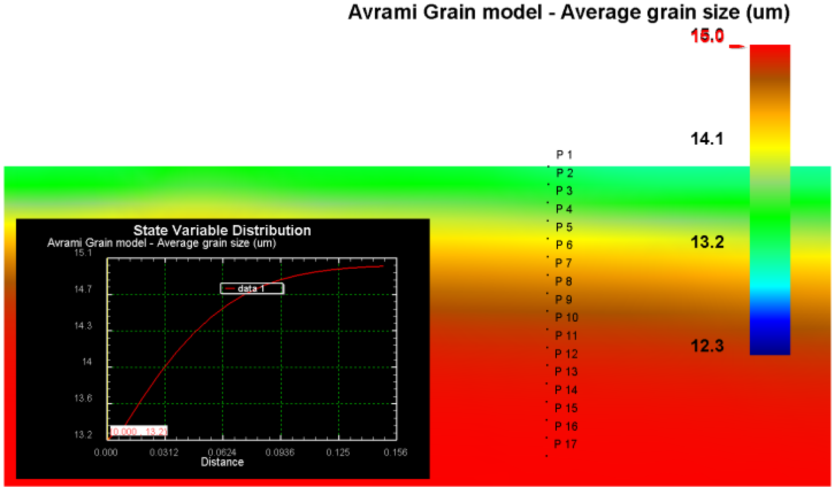
Avrami Grain model - Average grain size (um)
15.0
14.1
13.2
12.3
P 1
P 2
P 3
P 4
P 5
P 6
P 7
P 8
P 9
P 10
P 11
P 12
P 13
P 14
P 15
P 16
P 17
State Variable Distribution
Avrami Grain model - Average grain size (um)
15.1
14.7
14.3
14
13.6
13.2
data 1
0.000 13.2
0.000
0.0312
0.0624
0.0936
0.125
0.156
Distance

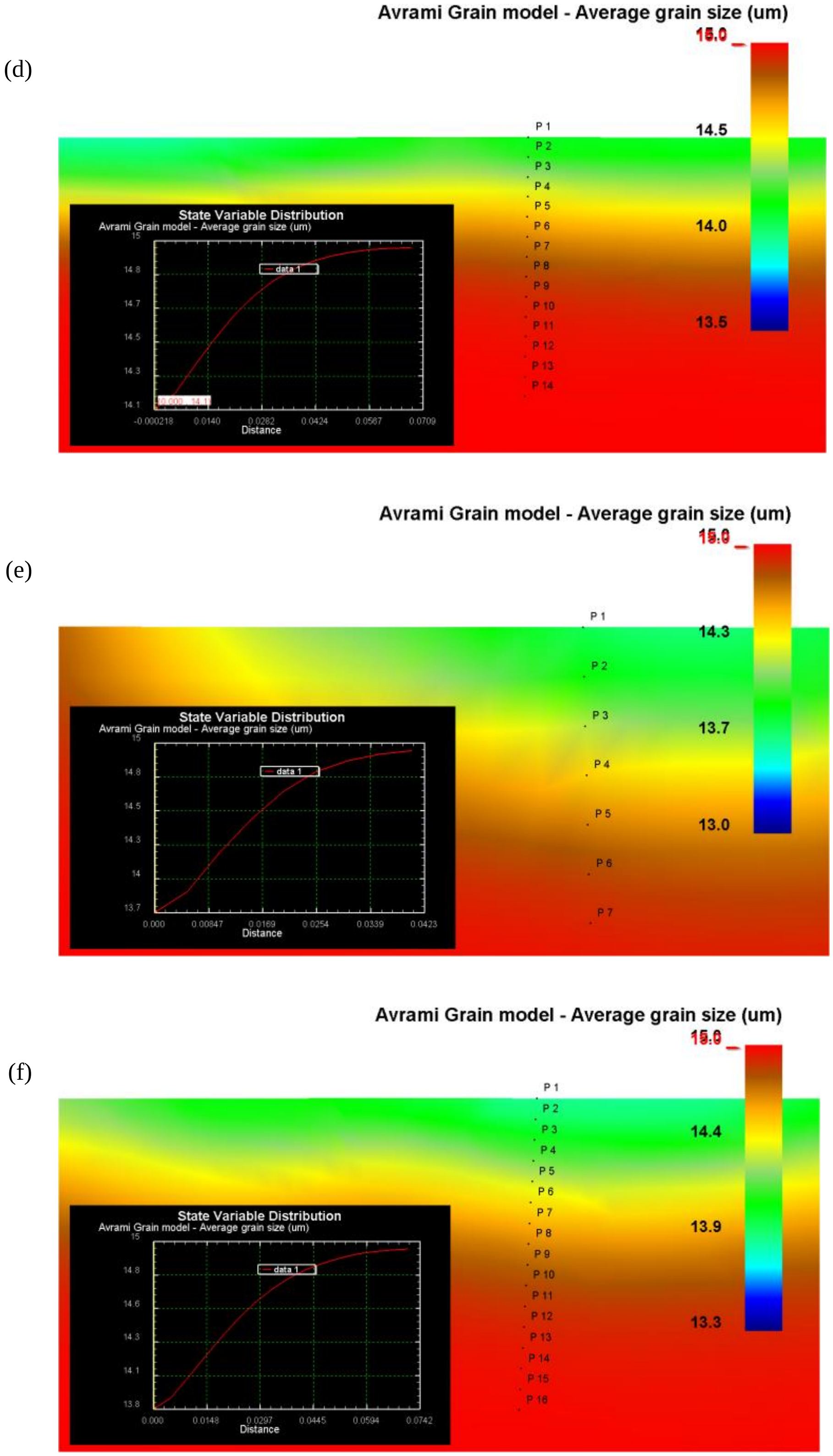

Fig. 4. The distribution of predicted AGS in the machined surface and subsurface and the variation of grain size with the depth below the machined surface for Test No. 1 using (a) JMAK 1, (b) JMAK 2, and (c) JMAK 3 and for Test No. 2 using (d) JMAK 1, (e) JMAK 2, and (f) JMAK 3.

depends on both d_{DRx} and X_{DRx}, where X_{DRx} is a function of ε as well as T and $\dot{\varepsilon}$. Similar to the analysis carried out above for d_{DRx}, it can be observed that the combined effects of temperature, strain and strain rate determine the final value of d_{avg}. Depending on the dominant T, ε or $\dot{\varepsilon}$, both d_{DRx} and d_{avg} can rise or diminish during machining with respect to the initial grain size.

4.2. Influence of tool edge radius

In this section, the input data including the JMAK constants, cutting conditions and tool geometry were the same as those of Ref. [7] as the first part of this research study was carried out as an extension of this reference. The variation of average grain size with tool edge radius including 0.005, 0.02, 0.03 and 0.04 mm is displayed in Fig. 5. As seen in this figure, the smallest AGS occurred for the lowest edge radius which is equal to 0.005 mm for both cutting conditions while AGS generally increased with tool edge radius. This can be attributed to the fact that by decreasing tool edge radius and sharpness of the tool, the contact area and heat transfer from the workpiece to the tool decrease, leading the temperature to increase in the workpiece and AGS to decrease. These results show that the proper tool edge radius leading to the finest grain size and better surface integrity in the machined surface was equal to 0.005 mm for Test Nos. 1 and 2. It should be noted that tools with the edge radius less than 0.02 mm are considered sharp tools.

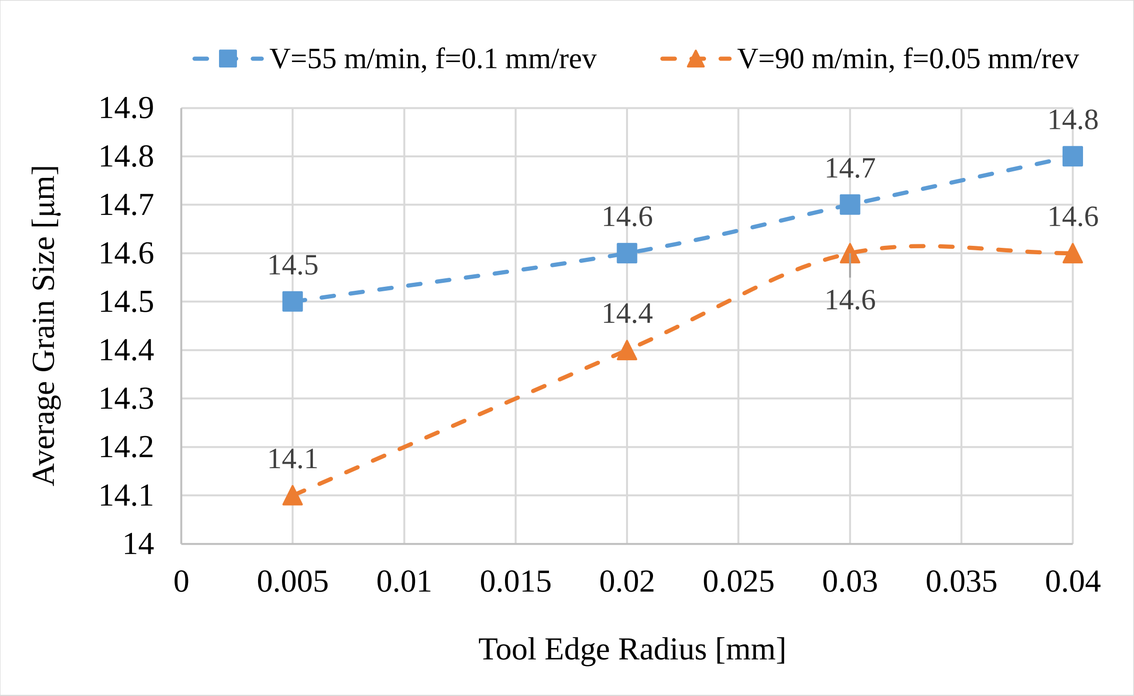

Fig. 5. The effect of tool edge radius on AGS.

Average grain size is plotted against the depth below the machined surface for various edge radii in Fig. 6. As observed in Fig. 6(a), AGS in both surface and subsurface of the machined workpiece rose with increasing tool edge radius for Test No. 1. The gradient of the variation of AGS with the depth under the machined surface also diminished by raising tool edge radius. In contrast, as viewed in Fig. 6(b) related to Test No. 2, AGS in the surface and subsurface of the machined workpiece was the lowest for the edge radius of 0.005 mm, whereas the surface and subsurface grain sizes for the edge radii of 0.02, 0.03, and 0.04 mm were almost the same. These results demonstrate that the grain size variation under the machined surface varied with changes in the cutting conditions.

4.3. Influence of rake angle

The variation of average grain size with rake angle including -15, -8, 0, +8, and +15 degrees is shown in Fig. 7. As observed in this figure, the minimum AGS occurred at the rake angles of -8 and 0 degrees for Test Nos. 1 and 2, respectively. This result shows that for the machining parameters under study, there was an optimum rake angle at which AGS was minimum. It is worth mentioning that the dissimilar behavior of AGS for the two tests can be attributed to interactions occurring among machining parameters [19]. This is known as interaction effects, when the effect of one factor (machining parameter) on the response (AGS) depends on the level of another factor(s) [20]. The interaction can be observed in Fig. 7, where the curves of the two tests are far from being parallel.

Figure 8 illustrates plots of average grain size with respect to the depth below the machined surface for various rake angles. As viewed in Fig. 8(a), AGS induced at negative rake angles were smaller than those at positive rake angles. This is in agreement with the results reported by [21], in which the effect of rake angle on grain size was investigated in orthogonal turning of aluminum alloy 6061-T6 for three rake angles of -15, +6, and +20 degrees. In addition, AGS did not change during machining when the rake angle of the tool was 15 degrees. This shows that the strain and temperature were not high enough to exceed the critical strain and temperature limit, respectively, to allow dynamic recrystallization to occur in cutting with a rake angle of +15 degrees.

Similar unpredictable, nonlinear behaviors of the variation of AGS with rake angle were observed for Test No. 2. For this cutting condition, when rake angle was 8 and 15 degrees, all the grain sizes in the surface and subsurface of the machined surface were 15 μm as there was no change in AGS during cutting. These results show that the grain size variation with tool rake angle had a more nonlinear behavior compared to tool edge radius.

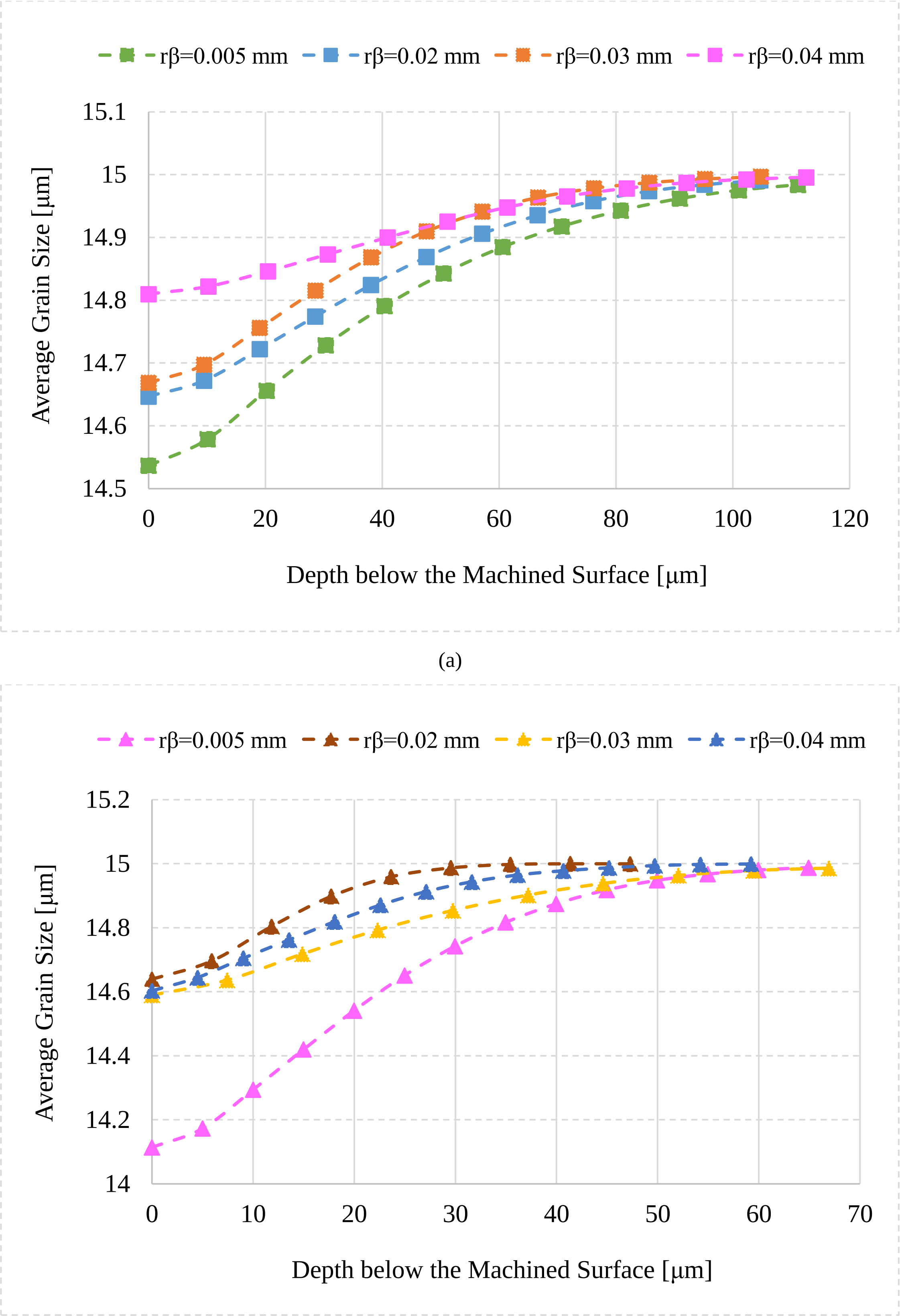

(a)

(b)

Fig. 6. The variation of AGS with depth under the machined surface for different tool edge radii (r_β) for (a) Test No. 1 and (b) Test No. 2.

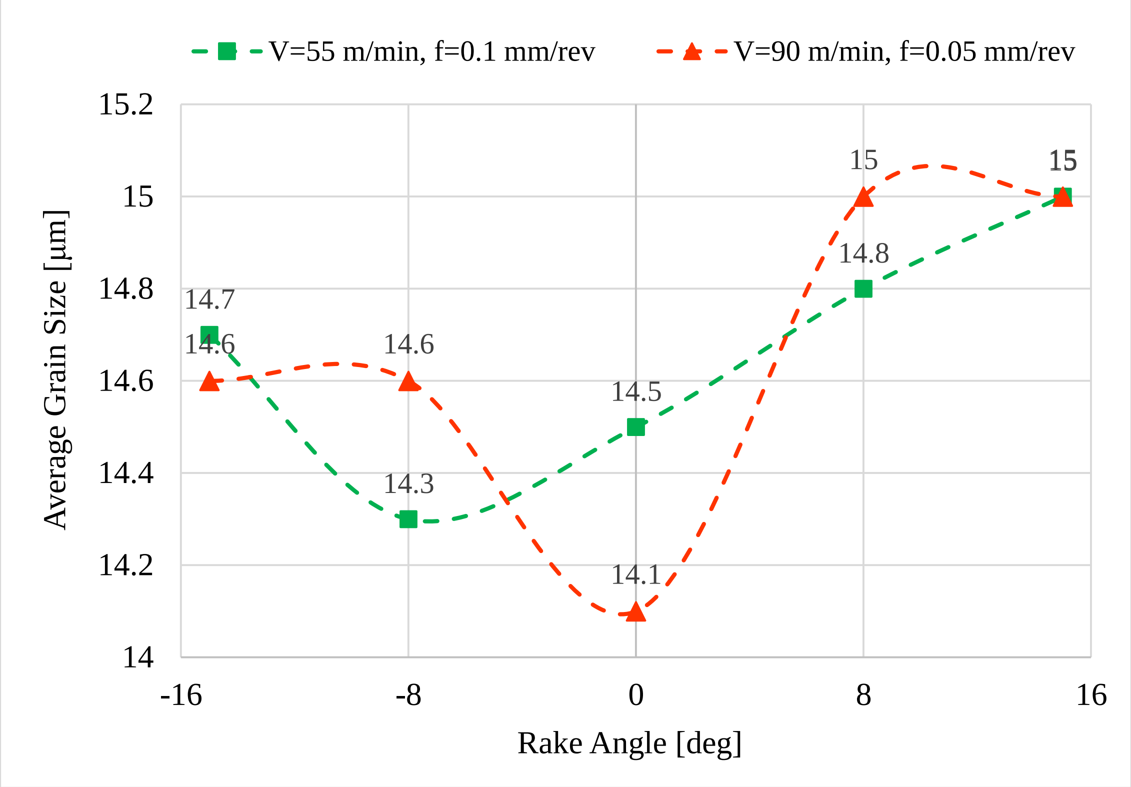

Fig. 7. The effect of rake angle on AGS for Test Nos. 1 and 2.

4.4. Analysis of Variance and regression modeling

The developed FE model combined with DoE and RSM can be effectively utilized to construct the response surface meta-models of average grain size (d), machining temperature (T), cutting force (F_C), and feed force (F_f) in terms of machining parameters. The 16 machining parameters in the D-optimal DoE and the corresponding simulation results of the above-mentioned responses are given in Table 6. The machining forces were averaged in the steady-state region. As observed in Table 6, MT changes from 732 to 1160 ℃ depending on the cutting condition and tool geometry, where MT was higher specially for negative rake angles. A negative rake angle causes high tool-chip contact pressure and friction, producing high frictional heat and a large MT [15,16]. In addition, previous research [5,22] have shown that high temperatures occurred during machining of Ti6Al4V alloy as a difficult-to-machine material. This can be attributed to the low thermal conductivity of Ti6Al4V alloy, which causes the generated heat to be entrapped in the cutting zone [23], leading to a higher MT. The FE predicted AGS, MT, CF, and FF for Run No. 10 (for instance) are given in Fig. 9. The 16 machining parameters and simulation results were utilized to quantify the effect of machining parameters on AGS, MT, CF, and FF using ANOVA and derive predictive quadratic models using RSM. The regression

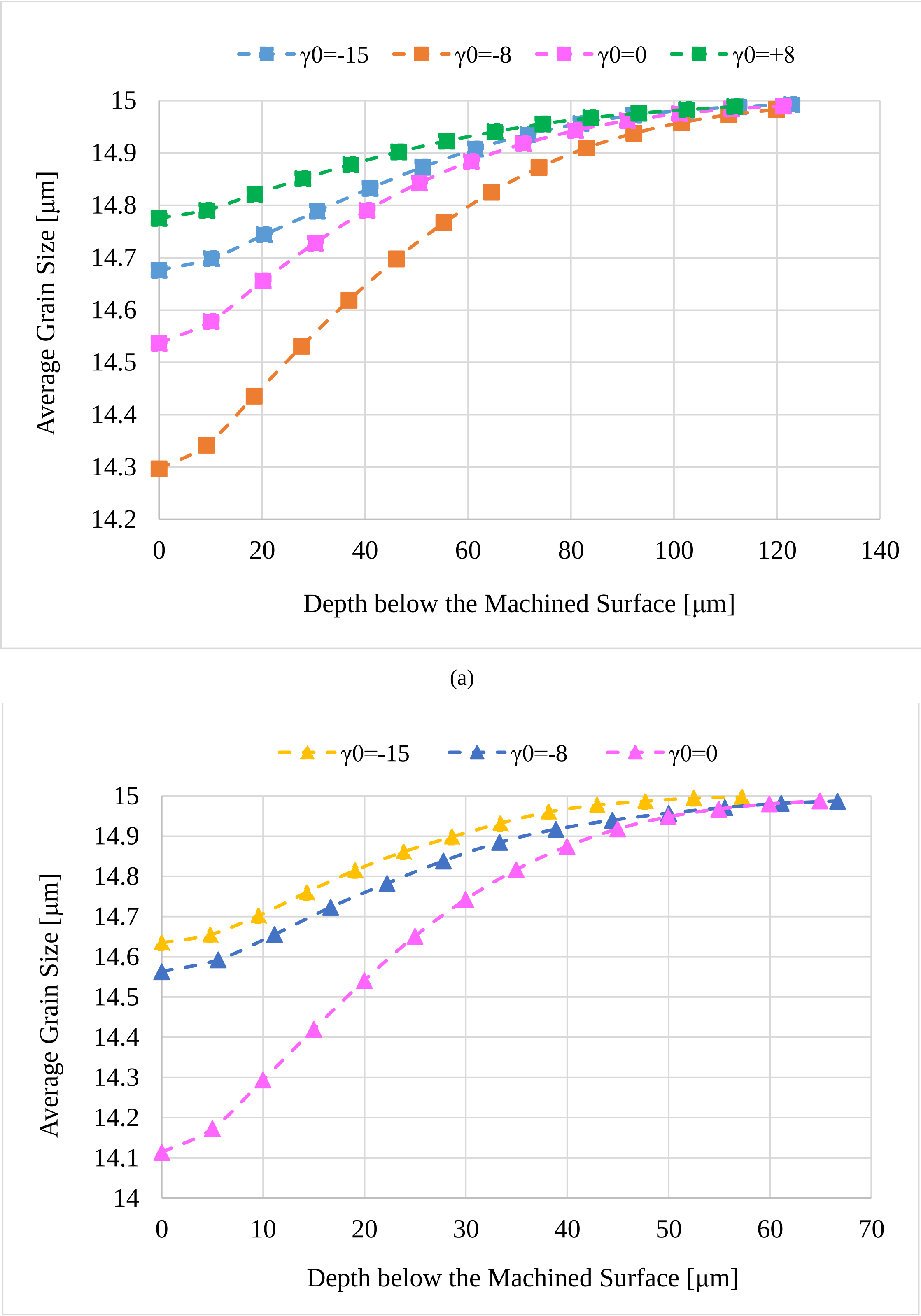

(a)

(b)

Fig. 8. The variation of AGS with depth under the machined surface for different rake angles (γ_0) for (a) Test No. 1 and (b) Test No. 2.

Table 6 Machining parameters using D-optimal DoE and the FE predicted AGS, MT, CF, and FF

Run No.	Cutting condition and tool geometry (Input)				Response (Output)			
	$V\ (m/min)$	$f\ (mm/rev)$	$r_\beta\ (mm)$	$\gamma_0\ (deg)$	$d\ (\mu m)$	T (°C)	$F_C\ (N)$	$F_f\ (N)$
1	55	0.1	0.005	15	15	747	129	31
2	90	0.1	0.005	-15	14.6	1140	373	255
3	55	0.075	0.005	-15	14.7	1020	306	276
4	90	0.075	0.005	11	15	894	113	28
5	72	0.05	0.04	0	14.7	898	141	127
6	90	0.075	0.04	-15	14.7	1140	335	308
7	55	0.1	0.02	0	14.5	1020	241	145
8	55	0.075	0.04	15	14.7	856	152	123
9	90	0.05	0.005	-15	14.6	1040	241	236
10	72	0.075	0.02	15	14.1	866	134	72
11	90	0.05	0.04	15	14.6	947	125	118
12	55	0.05	0.04	-15	14.6	918	176	162
13	55	0.05	0.005	15	15	732	94	26
14	81	0.1	0.03	-4	14.6	1150	372	244
15	60	0.1	0.04	-15	14.8	1160	394	320
16	90	0.1	0.04	15	14.7	1060	192	131

coefficients of the predictive models and the *P-value* results were obtained using the Design-Expert® software and are presented in Table 7. Using the ANOVA results, the significance (*P-value*) of machining parameters and their interactions and the accuracy of the regression models (*P-value*, R^2, R^2_{adj}, and *Adequate Precision*) were identified.

Based on the variance analysis at 95% confidence, the regression terms with *P* values less than 0.05 were considered to be Significant in the predictive models as the effect of these terms on the responses is significant. Non-significant terms identified through ANOVA were eliminated to improve the models. The more R^2 and R^2_{adj} are close to 1, the more accurate the model is. *Adequate Precision* measures the signal to noise ratio, where a ratio greater than 4 is desirable. As observed in Table 7, *P-values* of the regression models of AGS, MT, CF, and FF are, respectively, 0.0019, less than 0.0001, less than 0.0001, and 0.0007. All of these values are less than 5%, showing that the regression models are Significant. Moreover, considering that for all the responses, the R^2 and R^2_{adj} values are equal to or greater than 90% and the values of *Adequate Precision* are greater than 4, the predictive regression models are considered statistically precise [15,24-26] and can be used with a high level of confidence to predict AGS, MT, CF, and FF in the design space.

The ANOVA results revealed that rake angle was the most effective parameter influencing AGS and FF, while cutting speed had the smallest effect on AGS and FF in the design space, compared with the other machining parameters. Feed rate and tool edge radius also had the same contributions to changing AGS. In addition, cutting speed and rake angle had the highest effect on MT. In contrast, tool edge radius had the lowest influence on MT. Moreover, feed rate and rake angle were the most significant parameters influencing CF, whereas cutting speed was the lowest influential parameter affecting CF.

AGS, MT, CF, and FF can be formulated in terms of cutting speed $V(m/min)$, feed rate $f(mm/rev)$, tool edge radius $r_\beta(mm)$, and rake angle $\gamma_0(deg)$ using RSM by the second-order polynomial regression models whose coefficients are listed in Table 7. For instance, the quadratic model of AGS is given as:

$$\begin{gathered} d = 17.5907 - 0.058945 \times V - 0.626658 \times f - 97.9987 \times r_\beta + 0.012099 \times \gamma_0 \\ + 132.571 \times f \times r_\beta - 0.346246 \times r_\beta \times \gamma_0 + 0.000397 \times V^2 + 1890.59 \times {r_\beta}^2 \\ -0.001279 \times {\gamma_0}^2 \end{gathered} \tag{13}$$

where d is in terms of μm.

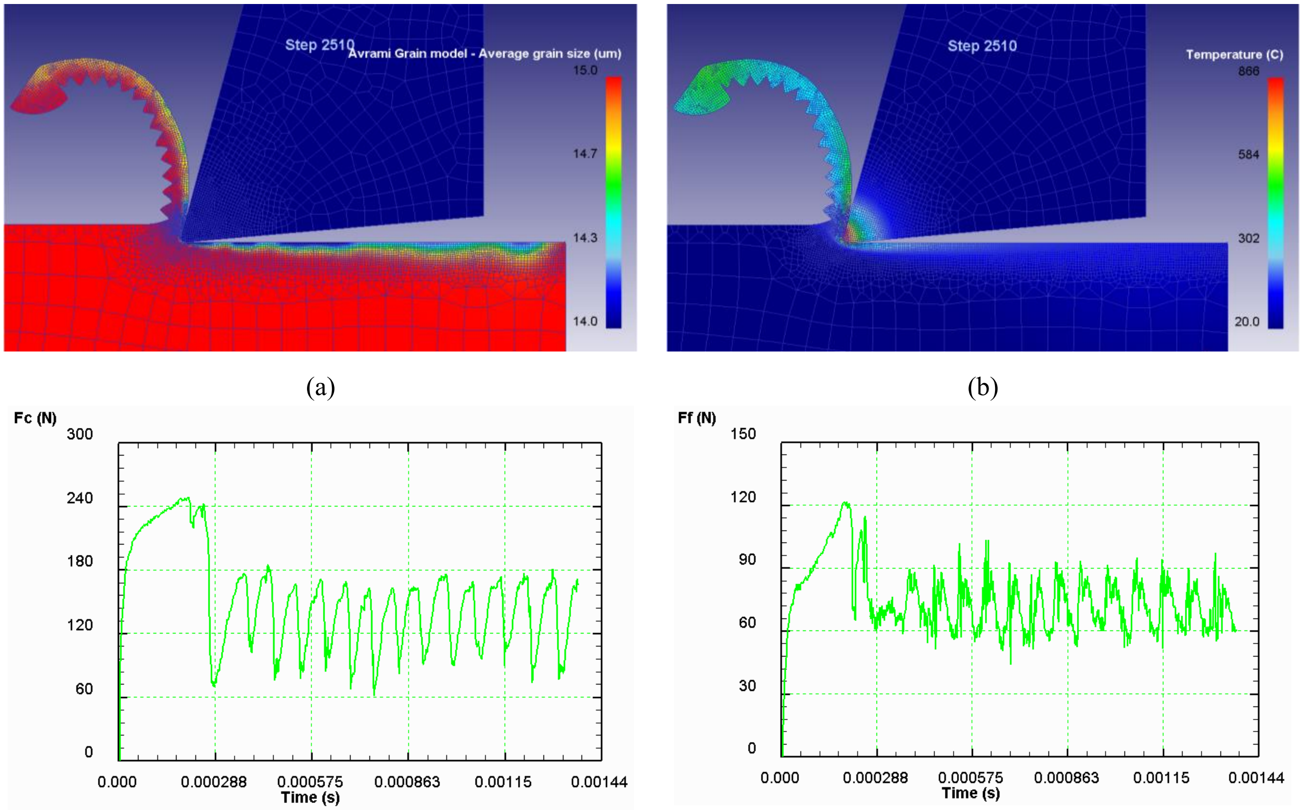

(a) (b)

(c) (d)

Fig. 9. The FE predicted (a) AGS, (b) MT, (c) CF, and (d) FF for Run No. 10.

4.5. Validation of the predictive regression models

Extra machining simulations named Run Nos. 17 and 18, which are listed in Table 8, were carried out within the space of the design of experiment in order to validate the predictive regression models. The simulated machining temperatures, cutting forces, feed forces, and average grain sizes for Run Nos. 17 and 18 are compared with those predicted using the regression models in Table 9. As observed in Table 9, there is good agreement between the results of FE simulations and regression predictions, indicating that the regression models are precise and can be confidently used to navigate the design space and predict AGS, MT, CF, and FF. The simulated AGS, MT, CF, and FF for Run No. 18 are displayed in Fig. 10.

Table 7 ANOVA for prediction of the regression models of AGS, MT, CF, and FF

Predictor	$d\ (\mu m)$		T (℃)		$F_C\ (N)$		$F_f\ (N)$	
	Coef.	P-value	Coef.	P-value	Coef.	P-value	Coef.	P-value
Intercept	17.5907		+1047.86		+57.60955		+74.66724	
V	-0.058945	0.3119	-9.68663	< 0.0001	+0.491166	0.3106	+0.935346	0.5489
f	-0.626658	0.0484	+863.92707	0.0001	+1447.84	< 0.0001	+1537.35	0.0363
r_β	-97.9987	0.0484	+3133.63	0.0003	-2471.99	0.1231	-5862.53	0.0110
γ_0	0.012099	0.0205	-6.93672	< 0.0001	-0.259698	< 0.0001	-4.53617	< 0.0001
$V \times f$	-	-	-	-	-	-	-24.07657	0.3001
$V \times r_\beta$	-	-	+25.37923	0.1036	-	-	+51.78835	0.1116
$V \times \gamma_0$	-	-	+0.045054	0.0347	-	-	-	-
$f \times r_\beta$	132.571	0.0568	+67633.41	0.0017	+42661.61	0.0694	+48985.32	0.0570
$f \times \gamma_0$	-	-	-71.468276	0.0031	-85.89090	0.0089	-52.80822	0.0846
$r_\beta \times \gamma_0$	-0.346246	0.0073	+90.73903	0.0031	+40.66644	0.2339	+86.81	0.0363
V^2	0.000397	0.1019	+0.084666	0.0631	-	-	-	-
f^2	-	-	-	-	-	-	-	-
${r_\beta}^2$	1890.59	0.0002	-170424.69	0.0074	-	-	-	-
${\gamma_0}^2$	-0.001279	0.0026	-	-	-	-	-	-
Model		0.0019		< 0.0001		< 0.0001		0.0007
Fit Statistics								
R^2		95.69 %		99.81		96.54		97.00
R^2_{adj}		89.21 %		99.29		93.52		92.51
Adequate Precision		15.40		41.67		17.11		14.20

Table 8 Machining parameters of validation tests

Run No.	$V\ (m/min)$	$f\ (mm/rev)$	$r_\beta\ (mm)$	$\gamma_0\ (deg)$	$\alpha_0\ (deg)$
17	64	0.085	0.01	-6	5
18	83	0.06	0.032	8	5

Table 9 FE simulations and regression predictions for validation of regression models

	FE Simulation				Regression Prediction			
Run No.	$d\ (\mu m)$	T (°C)	$F_C\ (N)$	$F_f\ (N)$	$d\ (\mu m)$	T (°C)	$F_C\ (N)$	$F_f\ (N)$
17	14.7	1040	290	207	14.6	1010	281	216
18	14.6	911	145	116	14.4	965	155	129

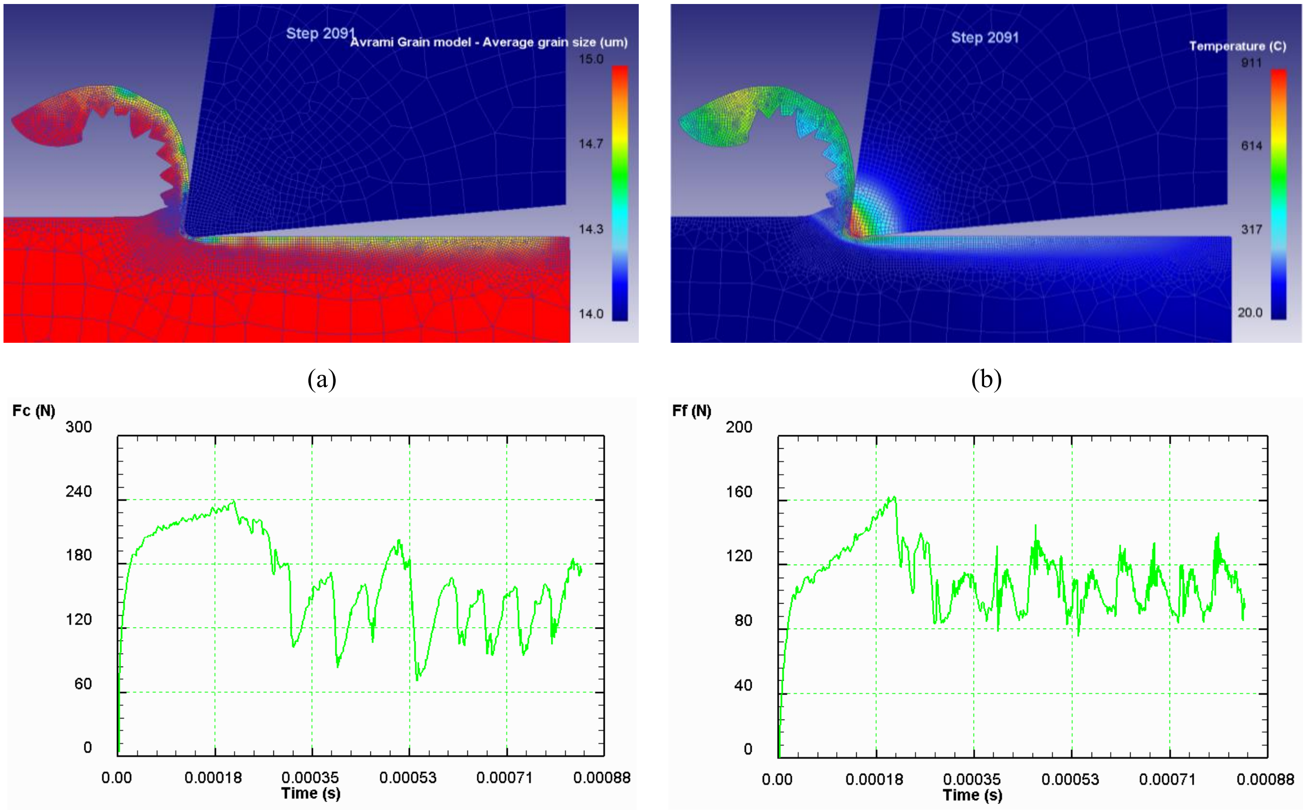

(a) (b)

(c) (d)

Fig. 10. The FE predicted (a) AGS, (b) MT, (c) CF, and (d) FF for Run No. 18.

4.6. Single-criterion optimization of AGS

The regression model for AGS was used in an optimization study to obtain optimum design solution for machining parameters as well as capturing the optimized AGS. The single-objective optimization problem is formulated as:

$$\begin{gathered}\text{Find } V, f, r_\beta, \text{ and } \gamma_0 \text{ to} \\ \text{Minimize } d \\ \text{Subject to } V_L - V \leq 0, V - V_U \leq 0, f_L - f \leq 0, f - f_U \leq 0, \\ {r_\beta}_L - r_\beta \leq 0, r_\beta - {r_\beta}_U \leq 0, {\gamma_0}_L - \gamma_0 \leq 0, \text{ and } \gamma_0 - {\gamma_0}_U \leq 0\end{gathered} \quad (14)$$

where V, f, r_β and γ_0 are the design variables, d is the objective function, and V_L, f_L, ${r_\beta}_L$ and ${\gamma_0}_L$ and V_U, f_U, ${r_\beta}_U$ and ${\gamma_0}_U$ are, respectively, the lower and upper bounds of the design variables in the design space. The optimization study was carried out based on a hill climbing technique using a penalty function approach which induces a hill to climb when the optimization starts in an undesirable location. In addition to the design points, a set of random points were checked to see if there was a more desirable solution [27]. Convergence was achieved and the optimal point was found when the distance between two consecutive objective functions or the change in the ratio of the two consecutive functions becomes less than 10^{-6} [27].

The optimum cutting speed, feed rate, tool edge radius, and rake angle together with the improved average grain size were captured and are provided in Table 10. Moreover, the contour maps of AGS are provided for the optimum solution for the significant interacting machining parameters including feed rate, tool edge radius and rake angle (as presented in Table 7) in Fig. 11. As observed in Fig. 11(a), AGS decreased for all the values of feed rate when tool edge radius approached a central value of 0.021 mm. In addition, as seen in Fig. 11(b), AGS diminished for all the negative, zero and positive values of rake angle when tool edge radius approached 0.021 mm. As reported in Table 10, the optimized AGS was 14.0 μm, showing a slight improvement compared with the smallest AGS equal to 14.1 μm for Run No. 10 in the DoE. However, the optimum values of machining parameters provided a material removal rate (MRR, $V \times f$) equal to 99.2 mm^3/s, which is larger than the MRR for Run No. 10 equal to 90 mm^3/s. This leads to less machining time and more productivity, which is highly suitable for the machining industry.

Table 10 Optimum machining parameters and AGS

$V\ (m/min)$	$f\ (mm/rev)$	$r_\beta\ (mm)$	$\gamma_0\ (deg)$	$d\ (\mu m)$
70	0.085	0.021	-15	14.0

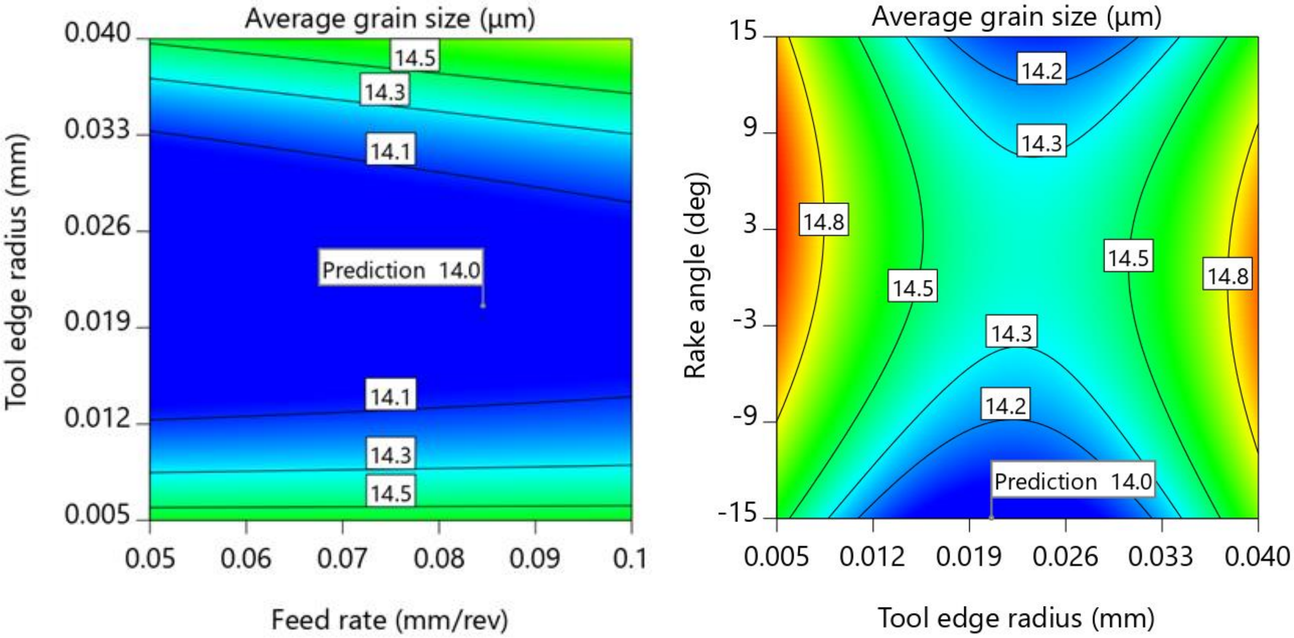

(a) (b)

Fig. 11. Contour plots of AGS for the optimum solution: (a) Feed rate and tool edge radius and (b) Tool edge radius and rake angle.

The optimum rake angle was -15 degrees. This is because a high negative rake angle leads to high tool-chip contact pressure and friction, producing high frictional heat and a large MT [15,16], which can lead to a smaller AGS. The optimal feed rate was equal to 0.085 mm/rev, close to the upper bound in the design space. A large feed rate results in a higher tool-chip contact area, and consequently, greater frictional heat and a higher MT [15,16], which can lead to a smaller AGS. A large feed rate also provides a larger MRR, yielding a lower MT, which can provide a larger AGS. In addition, a large feed rate leads to a higher strain rate in the workpiece during machining, which can produce a smaller AGS [28]. These processes compete to dominate the machining process. Tool edge radius approached a medium value of 0.021 mm at the optimum solution. It is recognized that by increasing tool edge radius, the contact area and frictional heat at the tool-chip-workpiece interfaces increase, resulting in a higher MT, which can lead to a lower AGS. In contrast, by increasing tool edge radius, the contact area and heat transfer from the workpiece to the tool increase, leading to less heat accumulation in the workpiece, which produces a lower MT and can lead to a larger AGS. In a machining process, these two processes compete to dominate. For the present optimum solution, tool edge radius converged to a medium value, showing that there is a balance between the two processes. Finally, the optimum cutting speed was obtained as 70 m/min, being a medium value in the design space. On the one hand, it is known that a high cutting speed generates larger frictional and plastic works, yielding a larger MT, which can produce a lower AGS. On the other hand, a high cutting speed causes a greater MRR, and consequently, larger heat evacuation and a smaller MT [15,16], which can result in a higher AGS. In addition, a large cutting speed results in a higher strain rate in the workpiece during machining, which can produce a smaller AGS [28]. In a machining process, there is a competition between these processes, depending on the magnitude of cutting speed [15]. In the present optimum solution, there is a balance between these processes, providing a medium value of cutting speed in the design space.

4.7. Multi-criteria optimization of AGS, MT, CF, and FF

The regression models of AGS, MT, CF, and FF were used to obtain optimum design solution for machining parameters and capture the optimized AGS, MT, CF, and FF. The multi-objective optimization problem is formulated as:

$$\begin{gathered}\text{Find } V, f, r_\beta, \text{ and } \gamma_0 \text{ to}\\ \text{Minimize } d, T, F_C, \text{ and } F_f\\ \text{Subject to } V_L - V \leq 0, V - V_U \leq 0, f_L - f \leq 0, f - f_U \leq 0,\\ {r_\beta}_L - r_\beta \leq 0, r_\beta - {r_\beta}_U \leq 0, {\gamma_0}_L - \gamma_0 \leq 0, \text{ and } \gamma_0 - {\gamma_0}_U \leq 0\end{gathered} \tag{15}$$

where V, f, r_β and γ_0 are the design variables, T, F_C, F_f, and d are the individual objective functions, and V_L, f_L, ${r_\beta}_L$ and ${\gamma_0}_L$ and V_U, f_U, ${r_\beta}_U$ and ${\gamma_0}_U$ are, respectively, the lower and upper bounds of the design variables in the design space.

The optimum cutting speed, feed rate, tool edge radius, and rake angle together with the improved AGS, MT, CF, and FF are provided in Table 11. Moreover, the contour maps of AGS, MT, CF, and FF are provided for the optimum solution in Fig. 12. Fig. 12(a) illustrates that AGS decreased for all the values of rake angle when tool edge radius approached a central value of 0.024 mm. In addition, as observed in Fig. 12(b), the variation of MT with feed rate was higher at larger tool edge radii. Fig. 12(c) displays that CF decreased with increasing rake angle for all the cutting speeds in the design space. Moreover, as seen in Fig. 12(d), FF increased with increasing feed rate at lower rake angles.

As reported in Table 11, the optimal value of AGS was 14.0 μm, showing a slight improvement with respect to the smallest AGS equal to 14.1 μm for Run No. 10 in the DoE. The optimized MT was 865 °C, which is almost equal to MT of Run No. 10, being equal to 866 °C. In addition, the optimum values of CF and FF were 104 and 65 N, which were lower than CF and FF of Run No. 10, being equal to 134 and 72 N, respectively. It needs mentioning that the MRR concerned with the optimal solution equaled 61.7 mm^3/s, which is smaller than the MRR for Run No. 10 equal to 90 mm^3/s.

Table 11 Optimum machining parameters and AGS, MT, CF, and FF

$V\ (m/min)$	$f\ (mm/rev)$	$r_\beta\ (mm)$	$\gamma_0\ (deg)$	$d\ (\mu m)$	T (°C)	$F_C\ (N)$	$F_f\ (N)$
74	0.05	0.024	15	.140	865	104	65

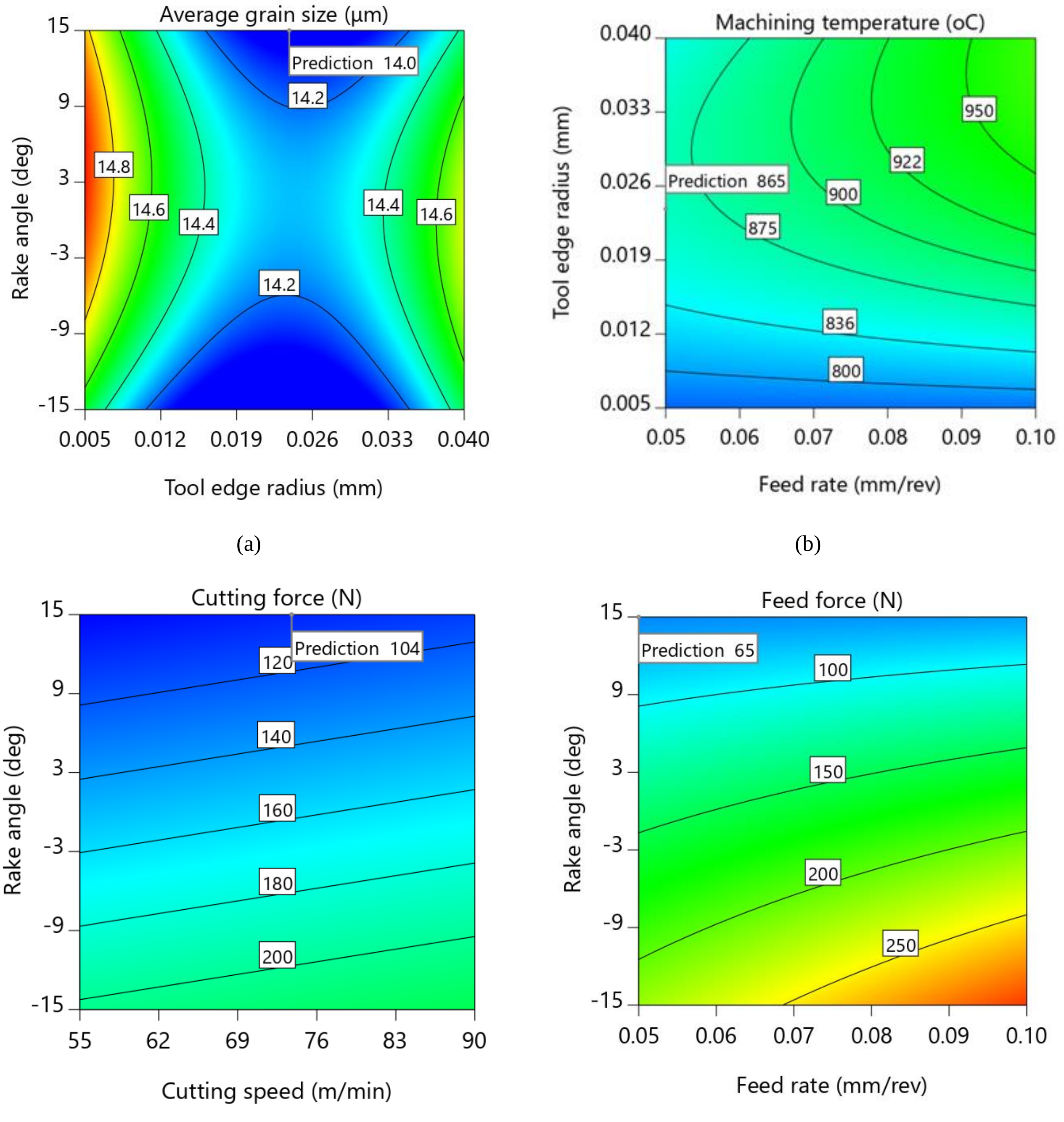

(a) (b)

(c) (d)

Fig. 12. Contour plots of AGS, MT, CF, and FF for the optimum solution of the multi-criteria optimization: (a) Tool edge radius and rake angle (b) Feed rate and tool edge radius, (c) Cutting speed and rake angle, and (d) Feed rate and rake angle.

Although MRR at the optimum solution decreased, all of the four responses of AGS, MT, CF, and FF as the individual objectives of the multi-criteria optimization problem generally improved. This is beneficial for the machining industry as high machining forces raise the power consumption of machine tools and result in an excessive deflection and consequently breakage of the tool, high machining temperature leads to inaccuracies in component dimensions, and both large machining forces and temperature cause high tool wear and damage [15,16].

The competing influences of machining parameters operating during a machining process can be considered to explain the optimization results. A high cutting speed generates larger frictional and plastic works, leading to more heat generation, which can produce a higher MT. This process, on the one hand, can result in more thermal softening and smaller CF and FF [15,16], and on the other hand, can lead to a smaller AGS, and consequently, a higher hardness and larger CF and FF. In contrast, a high cutting speed also leads to a greater MRR and more heat evacuation, which can produce a lower MT [15]. This, as explained earlier, can result in larger or smaller CF and FF. In addition to these processes, a large cutting speed results in a higher strain rate in the workpiece during machining, which can produce a smaller AGS and larger CF and FF. Therefore, the optimal value of cutting speed is determined based on the competition of these coupled thermo-mechanical processes.

A large feed rate results in a higher tool-chip contact area, and consequently, higher frictional heat, which can produce a higher MT. This can lead to more thermal softening and smaller CF and FF [15,16] or can result in a smaller AGS, a higher hardness, and larger CF and FF. A large feed rate also provides a higher MRR, which can yield a lower MT [15] and larger or smaller CF and FF. On the other hand, a large feed rate results in a higher strain rate in the workpiece, which can produce a smaller AGS [28] and larger CF and FF. Accordingly, feed rate is optimized based on the competition of these processes to rule the machining operation.

When tool edge radius is increased, the contact area and frictional heat at the tool-chip-workpiece interfaces increase, which can result in a higher MT. As explained earlier for cutting speed and feed rate, this not only can cause more thermal softening and smaller CF and FF, but also can lead to a higher hardness, and consequently, larger CF and FF. On the other hand, by increasing tool edge radius, the heat transfer from the workpiece to the tool rises, resulting in less heat accumulation in the workpiece, which can produce a smaller MT and a larger AGS, and therefore, a lower hardness and smaller CF and FF. In a machining process, the optimum value of tool edge radius is obtained depending on which of the above processes rules the machining operation.

A high negative rake angle causes high tool-chip contact pressure and friction, producing high frictional heat and a large MT [15,16]. This process not only can cause more thermal softening and smaller CF and FF, but also can lead to a smaller AGS, and consequently, a higher hardness and larger CF and FF. Depending on which process is dominant in the machining process, the magnitude of rake angle is determined.

5. Summary and conclusions

In the present research, the degree of accuracy of three series of JMAK constants in the finite element simulation of grain size alterations induced by orthogonal turning of Ti6Al4V alloy was evaluated. It was observed that all the three JMAK constants provided accurate results compared with the experimental ones, and as a result, all were reliable to be utilized for finite element predictions. Finite element simulations were carried out for a D-optimal DoE with four factors namely cutting speed, feed rate, tool edge radius and rake angle. ANOVA was conducted to capture the most influential machining parameters on the responses of AGS, MT, CF, and FF. The predictive regression models of AGS, MT, CF, and FF obtained using RSM were then utilized to capture the optimum machining parameters and improve the responses using the hill climbing optimization technique.

The ANOVA results demonstrated that rake angle was the highest effective parameter on AGS in the design space, followed by feed rate and tool edge radius which had the same impact on AGS. Cutting speed was the lowest influential parameter on AGS. In addition, cutting speed and rake angle had the highest impact on MT. In contrast, feed rate and rake angle were the most influential parameters affecting CF, whereas rake angle was the most significant parameter influencing FF. The results of the single-criterion optimization of AGS showed that machining of Ti6Al4V alloy using a sharp tool with a high negative rake angle produced the finest grains at a medium cutting speed and a large feed rate in the design space. Although the optimal value of AGS was slightly better than the smallest AGS in the DoE, the obtained optimum values of machining parameters led to a higher MRR and more productivity, which is beneficial to the machining industry. The results of the multi-criteria optimization of AGS, MT, CF, and FF demonstrated that machining of Ti6Al4V alloy with a tool having a medium cutting edge radius and high positive rake angle at a medium cutting speed and a low feed rate in the design space produced finer grains together with reduced CF and FF and unchanged MT, compared with the corresponding results for the machining condition providing the smallest grain in the DoE. This result is useful for the machining industry as low machining forces decrease the power consumption of machine tools and the probability of an excessive deflection and breakage of the tool, a confined machining temperature declines the probability of inaccuracies in component dimensions, and also both low machining forces and confined temperature cause less tool wear.

References

[1] Sadeghifar M, Sedaghati R, Jomaa W, Songmene V (2018) A comprehensive review of finite element modeling of orthogonal machining process: Chip formation and surface integrity predictions. Int J Adv Manuf Technol 96:3747-3791.

[2] Javidi A, Rieger U, Eichlseder W (2008) The effect of machining on the surface integrity and fatigue life. Int J Fatigue 30:2050-2055.

[3] Touazine H, Chadha K, Jahazi M, Bocher P (2019) Characterization of subsurface microstructural alterations induced by hard turning of Inconel 718. J Mater Eng Perform 28:7016-7024.

[4] Rotella G, Umbrello D (2014) Finite element modeling of microstructural changes in dry and cryogenic cutting of Ti6Al4V alloy. CIRP Ann Manuf Technol 63:69-72.

[5] Arısoy YM, Özel T (2015) Prediction of machining induced microstructure in Ti-6Al-4V alloy using 3-D FE-based simulations: Effects of tool micro-geometry, coating and cutting conditions. J Mater Process Technol 220:1-26.

[6] Wang Q, Liu Z, Wang B, Song Q, Wan Y (2016) Evolutions of grain size and micro-hardness during chip formation and machined surface generation for Ti-6Al-4V in high-speed machining. Int J Adv Manuf Technol 82:1725-1736.

[7] Pan Z, Liang SY, Garmestani H, Shih DS (2016) Prediction of machining-induced phase transformation and grain growth of Ti-6Al-4V alloy. Int J Adv Manuf Technol 87:859-866.

[8] Yameogo D, Haddag B, Makich H, Nouari M (2019) A physical behavior model including dynamic recrystallization and damage mechanisms for cutting process simulation of the titanium alloy Ti-6Al-4V. Int J Adv Manuf Technol 100:333-347.

[9] Ding H, Shin YC (2014) Dislocation density-based grain refinement modeling of orthogonal cutting of Titanium. J Manuf Sci Eng 136:041003-1- 041003-11.

[10] Liu R, Salahshoor M, Melkote SN, Marusich T (2015) A unified material model including dislocation drag and its application to simulation of orthogonal cutting of OFHC copper. J Mater Process Technol 216:328-338.

[11] Jafarian F, Umbrello D, Jabbaripour B (2016) Identification of new material model for machining simulation of Inconel 718 alloy and the effect of tool edge geometry on microstructure changes. Simul Model Pract Theory 66:273-284.

[12] Caruso S, Imbrogno S, Rinaldi S, Umbrello D (2017) Finite element modeling of microstructural changes in Waspaloy dry machining. Int J Adv Manuf Technol 89:227-240.

[13] Wu H, Ma J, Lei S (2018) FEM prediction of dislocation density and grain size evolution in high-speed machining of Al6061-T6 alloy using microgrooved cutting tools. Int J Adv Manuf Technol 95:4211-4227.

[14] Jafarian F, Masoudi S, Umbrello D, Filicec L (2019) New strategies for improvement of numerical model accuracy in machining of nickel-based alloy. Simul Model Pract Theory 94:134-148.

[15] Sadeghifar M, Sedaghati R, Jomaa W, Songmene V (2018) Finite element analysis and response surface method for robust multi-performance optimization of radial turning of hard 300M steel. Int J Adv Manuf Technol 94:2457-2474.

[16] Javidikia M, Sadeghifar M, Songmene V, Jahazi M (2020) On the impacts of tool geometry and cutting conditions in straight turning of Aluminum Alloys 6061-T6: An experimentally validated numerical study. Int J Adv Manuf Technol 106:4547-4565.

[17] Montenegro C, Abolghasem S, Osorio-Pinzon JC, Casas-Rodriguez JP (2020) Microstructure prediction in low and high strain deformation of Al6063 using artificial neural network and finite element simulation. Int J Adv Manuf Technol 106:2101-2117.

[18] DEFORM User's Manual, Version 11.2, 2017.

[19] Pawade RS, Joshi SS, Brahmankar PK (2008) Effect of machining parameters and cutting edge geometry on surface integrity of high-speed turned Inconel 718. Int J Mach Tool Manuf 48:15-28.

[20] Bradley N (2007) The response surface methodology, Indiana University South Bend, United States, MSc Thesis.

[21] Ding L, Zhang X, Liu CR (2014) Dislocation density and grain size evolution in the machining of Al6061-T6 Alloys. J Manuf Sci Eng 136:041020-1- 041020-10.

[22] Sima M, Özel T (2010) Modified material constitutive models for serrated chip formation simulations and experimental validation in machining of titanium alloy Ti-6Al-4V. Int J Mach Tool Manuf 50:943-960.

[23] Sadeghifar M (2017) Development of the analysis and optimization strategies for prediction of residual stresses induced by turning processes, Concordia University, Canada, PhD Dissertation.

[24] Capello E (2005) Residual stresses in turning: Part I: Influence of process parameters. J Mater Process Technol 160:221-228.

[25] Leppert T, Peng RL (2012) Residual stresses in surface layer after dry and MQL turning of AISI 316L steel. Prod Eng 6:367-374.

[26] Touazine H, Akab J, Jahazi M, Tahan A, Jomaa W, Bocher P (2017) Modeling of the microstructure alteration induced by hard turning of Inconel 718. Int J Adv Manuf Technol 93:3705-3712.

[27] Design-Expert User's Manual, Version 12, 2019.

[28] Jiao L, Miaoquan L, Weixin Y (2010) Microstructure evolution during high temperature deformation of Ti-6Al-4V alloy. Rare Metal Mat Eng 39:1323-1328.